Pergamon

Geochimica et Cosmochimica Acta, Vol. 59, No. 4, pp. 735–749, 1995

0016-7037/95 $9.50 + .00

0016-7037(95)00004-6

Relationship between surface structure, growth mechanism, and trace element incorporation in calcite

JEANNE PAQUETTE* and RICHARD J. REEDER

Department of Earth and Space Sciences, State University of New York at Stony Brook, Stony Brook, NY 11794-2100, USA

(*Received April* 26, 1994; *accepted in revised form November* 15, 1994)

Abstract—Crystal growth and coprecipitation experiments demonstrate the manner in which surface structure and, in turn, crystal structure influence growth mechanism and trace element incorporation in calcite. Dominant $\{10\bar{1}4\}$ faces grow by the spiral mechanism, producing asymmetric polygonized growth hillocks comprised of two pairs of nonequivalent vicinal faces. Trace elements Mg, Mn, and Sr are differentially incorporated into structurally distinct growth steps that comprise the nonequivalent vicinal faces. The resulting trace element distributions represent intrasectoral zoning patterns and are found to be consistent with face symmetry. Lateral spreading rates are also different for nonequivalent growth steps at a given degree of supersaturation, and the rate anisotropy is dependent on the Ca^{2+}:CO_3^{2-} ratio in the growth solution. A rounding transition associated with changes in kink site density occurs preferentially on only one pair of equivalent growth steps, further demonstrating the importance of step-specific kinetics and affinities on $\{10\bar{1}4\}$ faces.

Growth on other forms, including $\{01\bar{1}2\}$, $\{11\bar{2}0\}$, and $\{0001\}$, does not result in differential partitioning of trace elements and intrasectoral zoning, which is consistent with each of their surface symmetries and allowed growth mechanisms. However, sectoral zoning of Mg, Mn, and Sr occurs between these nonequivalent sectors, as well as $\{10\bar{1}4\}$.

We present a model detailing the geometry and coordination of elementary kink sites to explain both the differential incorporation and the rate anisotropy between nonequivalent growth steps on individual $\{10\bar{1}4\}$ faces. The model, constrained by face symmetry, accounts for affinities of different trace elements among four structurally distinct kink sites at which incorporation is preferred. The model also explains the observed differences in growth step velocity, as well as the in situ observations of growth step velocities by atomic force microscopy.

Trace element incorporation on the dominant $\{10\bar{1}4\}$ faces of calcite is controlled by the detailed structure of the interface, which varies spatially on a face, as well as with external conditions. Consequently, our observed trace element distributions violate equilibrium partitioning, and it is likely that many trace element distributions in natural carbonates also may not reflect equilibrium.

INTRODUCTION

Knowledge of the factors that control trace element incorporation in minerals has important applications in geochemical problems. In diagenetic studies of sedimentary rocks, the minor and trace element concentrations of calcite cements are commonly used to infer the composition of crystallizing fluids and the degree of water-rock interaction. However, experimental coprecipitation studies have shown that such approaches must take into account the kinetic factors affecting foreign ion partitioning between calcite and aqueous solutions (see Morse and Bender, 1990). Factors such as overall growth rates (e.g., Lorens, 1981; Mucci and Morse, 1983; Pingitore and Eastman, 1986; Dromgoole and Walter, 1990) and the activities of other foreign ions (Busenberg and Plummer, 1985; Pingitore and Eastman, 1986) are known to correlate with partition coefficients of minor and trace elements in calcite. Yet, in spite of the numerous studies of precipitation and dissolution kinetics of calcite, the fundamental controls on impurity incorporation during crystal growth remain poorly understood.

The influence of mineral surface structure on impurity distributions within single crystals has recently gained considerable attention. The widespread occurrence in natural and synthetic calcite of compositional sectoral zoning, i.e., compositional differences between time-equivalent sectors grown from crystallographically nonequivalent faces (e.g., Reeder and Grams, 1987; Reeder and Paquette, 1989; Raven and Dickson, 1989; Hendry and Marshall, 1991), and of intrasectoral zoning, i.e., compositional differences between time-equivalent portions of a given sector grown from a single face (Paquette and Reeder, 1990; Staudt et al., 1994), indicate clearly the importance of surface-structural controls on impurity incorporation during crystal growth. Intrasectoral zoning is especially useful, because it results from surface structural differences on a single face. For sectoral zoning, the compositional interface coincides with growth sector boundaries and emerges between faces at the crystal exterior. On the other hand, for intrasectoral zoning, the compositional interface coincides with boundaries (within a single growth sector) that emerge within a face at the crystal surface and separate regions of that face having different growth step structure. Because the distribution on a face of these regions having different growth step structure is controlled by the growth mechanism, which, in turn, is controlled by the interrelation of crystal surface structure and fluid chemistry, intrasectoral

* *Present address:* Department of Earth and Planetary Sciences, McGill University, Montreal H3A 2A7, Canada.

Table 1. Solution chemistry for selected calcite growth experiments.

	Low-Ca	Int.-Ca	High-Ca
Initial concentrations (M)			
Ca^{2+}	0.013	0.134	0.18
NH_4^+	0.50	0.512	0.70
Cl^-	0.526	0.780	1.06
Ionic strength (M)	0.53	0.92	1.21
pH range[1]	7.8-8.0	7.2-7.3	7.2-7.3
Alk_c range[2] (meq/L)	11.0-13.0	3.5-5.0	3.5-4.0
Ca^{2+}/CO_3^{2-} ratio range[3]	~ 100	~ 10^4	1.5-3.0 x 10^4
$\Omega_{calcite}$	~ 15	~10-19	~13-20

Notes:
1. The range of measured pH values following nucleation and addition of trace elements to solution.
2. Carbonate alkalinity determined by Gran titration of aliquots taken during growth. Values varied slightly during growth period.
3. The approximate free-ion ratio calculated at the onset of doping with trace elements. The ratio changed significantly over the duration of the experiment for low-Ca solutions and only minimally for high-Ca solutions (see text).

zoning offers a unique opportunity to identify the specific surface structural factors influencing impurity element incorporation. Furthermore, trace elements having different size, charge, and electronic configuration serve as sensitive probes of the surface incorporation sites.

The term surface structure is used here in a general sense and encompasses both atomic-scale details as well as larger physical features, such as growth steps, sometimes resolvable by light microscopy. Although they are interrelated, it is commonly necessary to distinguish among these features. Slice structure refers to the regular atomic arrangement of a thin slab of crystal at the surface parallel to a crystallographic face and whose thickness is the minimum necessary for a growth layer. This thickness coincides often, but not always, with d, the minimum repeat distance perpendicular to the face (Hartman, 1987). Each form, $\{hkl\}$, has a specific slice structure, identical for all its symmetry-equivalent faces. In the simplest case, the slice structure is identical to that of an equivalent slice from within the bulk structure. Certain crystalline solids, however, exhibit surface reconstruction or relaxation, which may cause changes in the size and shape of the surface unit cell relative to the bulk crystal (e.g., Somorjai, 1981).

Microscopic observations show that the actual surface exposed during crystal growth is not perfectly flat (e.g., Sunagawa, 1984, and references therein). In crystals grown from aqueous solutions, for example, some faces grow by a spiral mechanism, where emergence of screw dislocations provides continuous sources of steps. The random distribution of growth centers on the surface, the orientation of steps, their height, and spacing and density of kink sites, define an overall surface microtopography, which differs in detail from one crystal to the next. Each crystallographic form has a different microtopography, influenced by its slice structure and the specific growth conditions.

Partition coefficients between calcite and aqueous solutions are generally determined from coprecipitation experiments carried out in supersaturated aqueous solutions seeded with calcite powders and regulated by a chemostat technique to minimize the potential for compositional zoning within the synthetic overgrowth (e.g., Mucci and Morse, 1983; Dromgoole and Walter, 1990). Little attention is, therefore, given to the characterization and importance of the growth surface. To investigate the relationship of surface structure to trace element incorporation, we have grown synthetic calcite crystals up to several mm in size from room-temperature aqueous solutions and at various Ca^{2+} and CO_3^{2-} concentrations. Their growth surfaces (i.e., the active growth front at the time the experiment was interrupted) display microtopographic features, specific to each crystal form, many of which are resolvable by light microscopy. In calcite crystals grown in the presence of trace elements (Mg, Mn, and Sr), the correlation of trace element distributions with the microtopography provides valuable insight into the influence of surface structure on growth mechanisms and trace element incorporation. We propose a first-order model of incorporation sites that explains differential incorporation of divalent trace metal ions on calcite $\{10\bar{1}4\}$ and other forms. The findings explain complex trace element zoning patterns in calcite cement and illustrate the mechanism by which surfaces affect trace element distributions. More generally, the results demonstrate the path dependence of trace element incorporation and the need to consider their partitioning behavior in a kinetic or mechanistic framework, rather than solely a thermodynamic one.

MATERIALS AND METHODS

Growth Solution Chemistry

Solutions for the growth experiments were prepared by dissolving reagent-grade $CaCl_2 \cdot 2H_2O$ and NH_4Cl in deionized water with a re-

sistivity of 18 MΩ·cm. The initial Ca^{2+} concentrations of the solutions varied from 0.005 to 0.5 M, and their ionic strengths from 0.7 to 1.4 M, depending on the quantity of NH_4Cl added to optimize the growth of euhedral calcite single crystals (Table 1).

Solution pH was measured daily and carbonate alkalinity was monitored every 1–3 days by Gran titration of aliquots. For some experiments, total Ca and trace element concentrations of solution samples were determined by direct-current plasma spectrometry (DCP). In experiments with high initial Ca^{2+} concentrations (0.2–0.5 M), the large volume ratio of solution to crystals limited variations of Ca^{2+} concentration to less than 5% of its initial value over the three-week duration of a typical growth experiment. In other experiments, Ca^{2+} concentration dropped by as much as 50% over the same time interval. The distribution of aqueous species and the approximate saturation state of the solution with respect to calcite were estimated using the computer program EQ3NR (Wolery, 1983).

Crystal Growth Method

Synthetic calcite single crystals were grown by a modified version of a free-drift method described by Gruzensky (1967), where solid ammonium carbonate sublimates, and product NH_3 and CO_2 gases diffuse into an aqueous solution of calcium and ammonium chloride. This method yields optically clear, 0.3–2-mm single crystals over periods of 15–40 days.

For each experiment, 750–900 mL of Ca^{2+}-NH_4^+-Cl solution were transferred to a 1-L glass beaker covered by a Plexiglas plate, which was fitted with stopcocks to allow sampling without opening the vessel to the ambient atmosphere (Fig. 1). The vessels were immersed in a water bath to maintain the solutions at a constant temperature of 28°C (±2°C), and the solutions were left unstirred during the experiments.

Trace elements, Mn, Mg, and Sr, were added separately or in various combinations during the course of each coprecipitation experiment in the form of aqueous solutions of chloride salts. The compositions of the dopant solutions were adjusted to obtain concentrations in the range 100–2500 ppm that were suitable for analysis. The addition of Mn, Mg, and Sr to solution generally decreased growth rates somewhat (cf. Dromgoole and Walter, 1990).

The solution pH, initially slightly acidic (pH 5.5–5.7), increased over the first two days, until the solution reached a supersaturation of 20–30 times with respect to calcite (pH 7.5–7.8). Within the next 12 h, calcite crystals nucleated at the surface of the solution, on the substrate provided by the beaker walls and by Tygon or glass tubing immersed in solution. The pH dropped sharply to values of 7.2–7.4 with the onset of nucleation and rapid initial crystal growth. After this point, the solution remained at a nearly constant pH and degree of supersaturation (depending on the initial Ca^{2+}), controlled largely by the rate of gas supply to the system by sublimation. In some experiments, a slight vertical pH gradient in the solution (up to 0.5 pH units over 6–8 cm) persisted as long as the source of solid $(NH_4)_2CO_3$ was left in place. The resulting gradient in supersaturation within the solution influenced the size and, to a lesser extent, the habit of calcite crystals growing at different depths below the solution surface.

In some experiments, the pH and degree of supersaturation were modified at known intervals by adding dissolved $(NH_4)_2CO_3$ to the solution, or by removing and restoring the bottle containing sublimating solid $(NH_4)_2CO_3$ from the assembly. For certain experiments, sections of tubing on which calcite single crystals had precipitated were transferred to sealed beakers containing Ca^{2+}-NH_4^+-CL^- solutions titrated with an aqueous solution of ammonium carbonate to desired values of carbonate alkalinity. This method decreased the development of significant pH gradients. Carbonate alkalinity and pH measurements indicate that, in these experiments, the large ratio of solution to crystal surface area resulted in a nearly constant ratio of Ca^{2+}:CO_3^{2-} concentrations over periods of up to two weeks. After each growth experiment, the Tygon or glass tubing was quickly removed and either air-dried or rinsed in anhydrous alcohol, providing the best source of single crystals.

Cathodoluminescence (CL) microscopy

The addition of Mn^{2+} to growth solutions resulted in the development of concentric zoning that was imaged using CL microscopy.

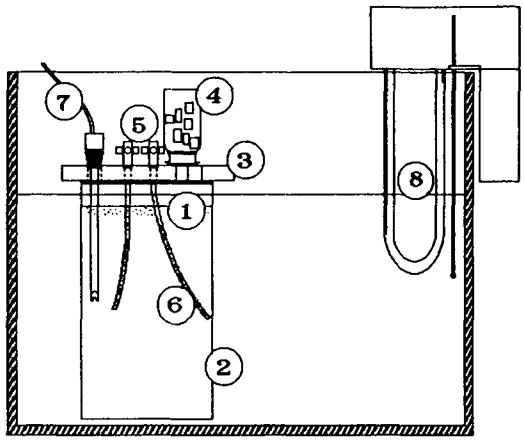

FIG. 1. Schematic diagram of the system used for growth of the calcite crystals. 1 = solution-vapor interface; 2 = 1 L Pyrex vessel; 3 = Plexiglas plate sealing vessel; 4 = container holding solid $(NH_4)_2CO_3$ fixed over opening in plate; 5 = ports for sampling and doping; 6 = Tygon or glass tubing used as substrate; 7 = port for pH measurements; 8 = immersion heater with temperature controller for water bath.

Observations were made on a Technosyn cold-cathode luminescence microscope operated at 11–15 kV. This technique provides qualitative compositional maps of the geometry of the different zoning patterns on growth surfaces, as well as in sections through Mn-bearing synthetic crystals. Concentric zoning also provides a record of growth habit. Changes in solution composition induced by addition of other trace elements or carbonate ions during crystal growth induced a similar chemical stratigraphy, although not evident in CL of Mn-free crystals.

CL photomicrographs were used in electron probe and synchrotron X-ray fluorescence analyses to establish time equivalence for documenting concentration differences between and within sectors. This also allowed for correlation of changes in crystal composition with solution chemistry.

Electron probe microanalysis (EPMA)

Concentrations of Mg, Mn, Sr, and Ca were determined using a Cameca Camebax electron microprobe. An accelerating voltage of 15 kV was used for analysis of Ca and Mg, and 30 kV for Mn and Sr, both with a beam current of 15 nA. A beam size of approximately 15 μm was used on specimens and standards to minimize volatilization. Ten replicate analyses (each for 30 s) were made of each spot with no indication of a systematic increase or decrease of count rate that might suggest volatilization. Homogeneous natural carbonate minerals of known composition were used as standards, and full-matrix correction methods were employed for data reduction. Minimum detection limits were approximately 50 ppm for Mn and Mg and approximately 100 ppm for Sr. 95% confidence limits for reported concentrations are typically 50–100 ppm for Mg and Mn and 100–200 ppm for Sr. Iron was below detection limit in all synthetic calcite crystals analyzed.

Trace element analyses were performed on thin sections prepared by mounting oriented single crystals of synthetic calcite in epoxy on standard petrographic thin sections, and polishing them to intersect the compositional zones and growth sectors of interest. Cathodoluminescence micrographs were used to locate spot analyses in relation to the different sectors and concentric zones.

Synchrotron X-ray fluorescence microanalysis (SXRFMA)

Manganese and Sr concentrations of several synthetic calcite crystals were also investigated by synchrotron X-ray fluorescence microanalysis (SXRFMA) at the X26A beamline of the National Synchrotron Light Source at Brookhaven National Laboratory. Because of

the relatively large beam size (approximately 10 × 10 μm) and extreme penetration (incident hard X-rays penetrate the entire sample thickness), sampling volumes for each SXRFMA analysis were limited by sample thickness, so that exact comparisons with EPMA data are generally not possible.

For SXRFMA all sample sections were mounted on ultra high-purity silica glass or single-crystal quartz slides. Sections through crystals were mounted in epoxy and cut and polished with a final grade of 0.3-μm alumina to thicknesses of 25–50 μm. Surface sections were cut and ground from the back to produce sections (typically 50 μm) in which the growth surface is preserved and faces up. Pairs of CL and light photomicrographs of crystals were used to position the beam on the zones and sectors of interest. The SXRFMA experiments were carried out in air. A 19.2 mm-thick Kapton filter placed between the sample and the detector reduced the intensity of the Ca *K* lines, allowing the higher energy X-rays from trace elements to emerge from the background (cf. Lu et al., 1989). Acquisition times were typically 300 s. Peak areas (generally, *K* lines) for selected elements were obtained from a graphical peak-fitting program.

Elemental concentrations were obtained using the so-called standardless method by comparing the peak area ratio Tr/Ca (where Tr = trace element of interest) to that calculated by the X-ray fluorescence program NRLXRF adapted for the specific energy spectrum of the synchrotron source (Lu et al., 1989). Variable parameters were calibrated using two standards (anorthite glass and calcite), yielding comparable results. SXRFMA also revealed the presence of accidental contaminants (Zn, Pb, Fe) in trace amounts (<50 ppm) that were below the detection limits of EPMA (Paquette, 1991). On the basis of net counts and background counts, minimum detection levels for SXRFMA with the procedures used here are in the range 1–3 ppm for Mn and Sr, and relative precisions are better than 1%.

Surface characterization of synthetic crystals

Crystallographic forms were indexed from interfacial angles measured directly from photomicrographs of oriented crystals and compared to those of forms plotted with the computer program ATOMS (Dowty, 1989). In some cases, the irregular or curved character of faces prevented their precise indexing. Differential interference contrast (DIC) microscopy and reflected-light microscopy were used to image the microtopography of the growth surfaces.

RESULTS

Growth experiments were designed to span a range of initial total Ca^{2+} concentrations of the parent solution, from 0.005–0.5 M. The approximate range of supersaturation relative to pure calcite spanned by different experiments was eight to twenty times, while their Ca^{2+}:CO_3^{2-} (free ion) concentration ratio varied from approximately 100 to 30,000. Solution data from selected experiments are presented in Table 1. We make no attempt here to describe results systematically over the entire range of initial Ca^{2+} concentrations, supersaturation states, and Ca^{2+}:CO_3^{2-}; rather, we focus on the general incorporation patterns of the trace elements and their relationship to surface structure and growth mechanism.

The calcite crystals grown are optically clear, single, and untwinned. Average growth rates normal to faces were approximately 1–5 × 10^{-8} cm/s. The overall crystal morphology varied appreciably over the range of Ca^{2+}:CO_3^{2-} concentration ratios and degree of supersaturation of the solutions, even in the absence of trace elements. All crystals examined from a given growth experiment showed the same combination of dominant forms. In individual crystals, the record of crystal morphology preserved by compositional concentric zoning indicates that the dominant forms persisted throughout most of their growth history.

Zoning Geometry

The introduction of Mn^{2+}, Mg^{2+}, and Sr^{2+} during growth resulted in the development of three distinct types of zoning. The geometry and spatial arrangement of these zoning patterns were most easily recognized for Mn^{2+} using CL microscopy. As noted previously, concentric zoning, where the compositional interface, parallel to the growth surface, may be sharp or gradational, records the position and morphology of the advancing growth front at successive stages during growth. In our experiments, concentric zoning could generally be related to changes in bulk fluid properties (e.g., addition of trace elements, Ca^{2+}, or CO_3^{2-}), and it defined a CL stratigraphy that could be correlated between all crystals from a given experiment. In rare cases, however, a specific type of concentric zoning pattern appeared, displaying repetitive, fine-scale concentric zones, generally less than 5 μm thick. This oscillatory zoning, similar to that documented by Reeder et al. (1990), could not be correlated between different crystals and was unrelated to obvious changes in fluid chemistry or system parameters. Regardless of its origin, however, concentric zoning provided time markers that were essential for documenting the two types of sector-related zoning described below.

Growth on different faces leads to the development of sectors within crystals. In the present work, nonequivalent forms exhibit different affinities for incorporation of trace elements, resulting in sectoral zoning (cf. Reeder and Paquette, 1989). Compositional interfaces for sectoral zoning coincide with growth sector boundaries.

The third type of zoning, which is the principal focus of the present work, occurs between time-equivalent portions within individual $10\bar{1}4$ sectors, the only sector type in which it occurs. Paquette and Reeder (1990) called this intrasectoral zoning to distinguish it from sectoral zoning. In sectors where it occurs, the presence of straight concentric zones (readily visible in Mn^{2+}-doped crystals by CL) throughout the time-equivalent portions of $10\bar{1}4$ sectors clearly indicates that the entire sector grew from a unique ($10\bar{1}4$) face. The sharp compositional interface of intrasectoral zoning, therefore, cuts across concentric zoning within $10\bar{1}4$ sectors.

Throughout our study, the relationship between intrasectoral zoning and the surface microtopography of {$10\bar{1}4$} was established by direct comparison of DIC and reflected-light images of growth surfaces with corresponding CL micrographs and EPMA and SXRFMA data of the same surfaces. Further correlations were made after sectioning through crystals in orientations both parallel and perpendicular to {$10\bar{1}4$} surfaces. Persistence of the intrasectoral zoning pattern from the surfaces into progressively younger portions of the sectors demonstrates that this zoning type is created as the surface advances during growth (cf. Fig. 18.4a–c of Paquette et al., 1993).

Correlation of Trace Element Incorporation with Surface Microtopography

The {$10\bar{1}4$} rhombohedron

This rhombohedron, parallel to the perfect cleavage, is the only growth form that persists over the entire range of solution

compositions investigated. It is also the dominant form at higher supersaturation. Growth surfaces are typically flat and smooth in appearance, but in DIC microscopy and in reflected-oblique illumination, they are seen to contain shallow pyramids called growth hillocks (Fig. 2), similar to those commonly observed on mineral and nonmineral crystal surfaces, and which are indicative of growth by the spiral mechanism (cf. Sunagawa, 1984). Each hillock consists of three or four vicinal faces (i.e., nonrational faces deviating only slightly in orientation from an ideal ($10\bar{1}4$) face). The distribution of individual hillocks is random on any given ($10\bar{1}4$) face. If several hillocks are present on a face, their geometries are identical (Fig. 2), although their sizes may differ. On crystals grown at moderate to low supersaturation, $\Omega \approx 8$–12, a single hillock may cover an entire crystal face (Fig. 3). In most cases, the topography on growth hillocks, as recorded by concentric zoning in thin sections at high angle to $\{10\bar{1}4\}$ faces, cannot be resolved by CL microscopy, indicating that the summits of hillocks rise less than 5 μm above the overall ($10\bar{1}4$) face. Consequently, the inclination of a typical vicinal face deviates only one degree or less from that of ($10\bar{1}4$).

Some vicinal faces of growth hillocks clearly show macrosteps that are parallel to the edges of the cleavage rhombohedron (Fig. 3), and therefore have directions $\langle\bar{4}41\rangle$. The featureless areas between macrosteps are the expression of more or less evenly spaced steps, parallel to the macrosteps, but of smaller heights (as low as 3 Å) that could not be resolved by reflected-light or DIC microscopy. Atomic force microscopy on calcite $\{10\bar{1}4\}$ surfaces grown by the same method has shown that 3 Å steps are present on these vicinal faces and are parallel to the macrosteps (Reeder and Hochella, 1991; and J. Paquette and R. J. Reeder, unpublished work). In situ atomic force microscopy (Gratz et al., 1993; Dove and Hochella, 1993) has confirmed that layer growth on calcite $\{10\bar{1}4\}$ surfaces occurs by advance of relatively straight step segments having the orientations described above and heights of 3 Å, or small multiples thereof.

CL microscopy reveals that, on Mn^{2+}-doped crystals, the luminescence intensities differ markedly among specific pairs of vicinal faces on each hillock (Fig. 3b, d). Vicinal faces marked a and b in Fig. 4 always show dull luminescence relative to those marked a' and b'. Qualitatively, this difference in CL indicates that the material comprising vicinal faces a' and b' (and in the near surface below) is enriched in Mn relative to that comprising a and b. Vicinal faces a and b show luminescence intensities that are indistinguishable from one another, and the same is true of vicinal faces a' and b'. The same zoning pattern is evident on all hillocks on $\{10\bar{1}4\}$ faces of a given crystal, and, allowing for minor variations in absolute intensities, on all crystals in an experiment. The reverse CL trend, in which vicinal faces a and b show brighter luminescence than a' and b', is never observed. Consequently, on the basis of these qualitative observations, Mn consistently exhibits a greater affinity for incorporation into vicinal faces a' and b' than into a and b during growth.

Hillock morphology and the zoning patterns on their vicinal faces (as imaged by CL microscopy) are found to obey the face symmetry of $\{10\bar{1}4\}$, a c-glide. Vicinal faces that are related by the c-glide (i.e., a and b are related to one another, and a' and b' are related) show identical luminescence characteristics and trace element distributions; the vicinal faces not related by symmetry (e.g., a and a') show different characteristics.

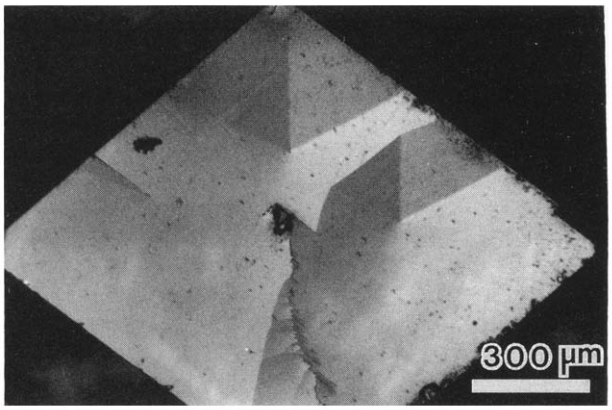

FIG. 2. DIC image of a ($10\bar{1}4$) growth surface of a synthetic calcite crystal oriented with the c-glide vertical. Two growth hillocks, having identical geometry, are present on the upper and upper-right portion of the face, and separated by a large macrostep. Hillocks contain three vicinal faces. The upper portion of the hillock is polygonized, whereas the lower portion is conical in shape.

The trace element distribution observed near the surface is also found to exist at depth below the surface. By sequentially polishing down through a ($10\bar{1}4$) growth surface, the same CL pattern outlining the contact between nonequivalent vicinal faces persists at depth within the crystal, giving rise to an intrasectoral zoning pattern. In sections through a given sector, perpendicular to the growth face, a continuous sequence of time-equivalent portions reveals the distinct difference in CL that corresponds to nonequivalent subsectors (i.e., regions of growth sector that formed from specific vicinal faces; Fig. 5). This geometry, observed in different perspectives, is consistent with spiral growth in which vicinal faces remained distinct and were arranged essentially as they appear on the final growth surface. Thus, intrasectoral zoning is the record (in the bulk crystal) of differential incorporation that occurred at the surface during growth.

EPMA and SXRFMA data confirm the differences in Mn distributions that are qualitatively indicated by CL; the data also demonstrate that systematic differences exist for Mg and Sr. SXRFMA probe traverses (Fig. 6a,b) across nonequivalent vicinal faces of a growth hillock show distinct differences in Mn and Sr concentrations in the associated subsectors. For these traverses, thin sections were made parallel to and bounded by a ($10\bar{1}4$) growth surface containing a single large growth hillock, mounted face-up on an ultra high-purity silica glass disk. The abrupt changes in Mn and Sr concentration correspond directly with the boundary separating nonequivalent vicinal faces on the hillocks. In all such traverses of hillocks, subsectors associated with vicinal faces a' and b' are always enriched in Mn and depleted in Sr, relative to those associated with vicinal faces a and b. That relative distribution of Mn is consistent with CL observations. Mn concentrations in equivalent subsectors (e.g., a and b) are identical within error; the same is true for Sr. Because the sample section has a finite thickness (~50 μm), the concentrations shown in Fig.

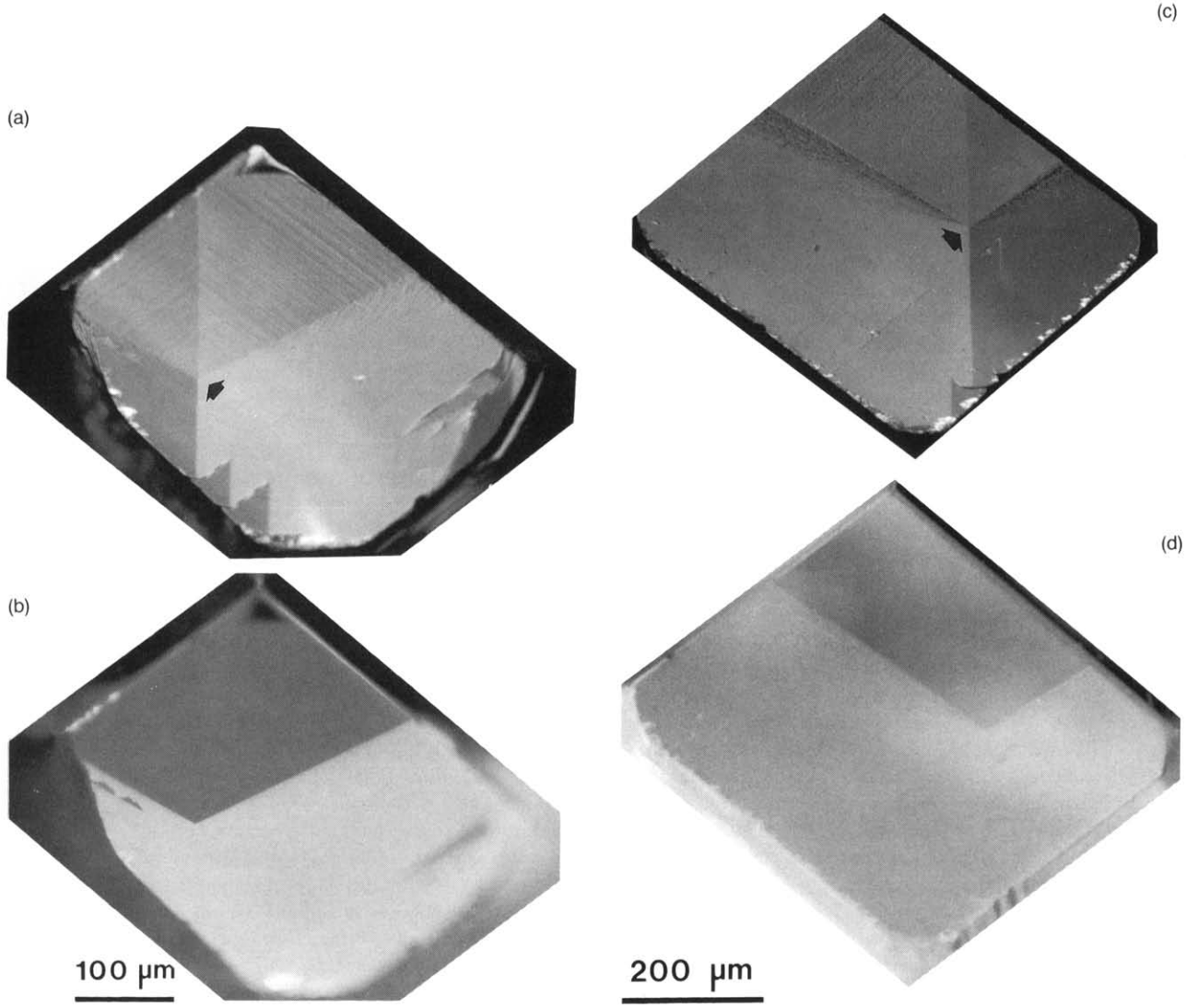

FIG. 3. (a) DIC image of a $(10\bar{1}4)$ growth surface of a Mn-doped synthetic calcite crystal grown at an intermediate Ca^{2+}:CO_3^{2+} ratio. A single polygonized growth hillock dominates the face. The arrow marks the summit of the hillock, and the four vicinal faces are separated by sharp edges. The face orientation and the vicinal face designations are as shown in Fig. 4. Straight macrosteps are visible on the two upper vicinal faces. (b) CL image of the same face in (a). Mn-activated luminescence is bright in the area comprised by the lower vicinal faces and dull in the upper two. (c) DIC and (d) CL images of a single polygonized hillock on a $(10\bar{1}4)$ growth surface of a Mn-doped synthetic calcite crystal grown at a relatively high Ca^{2+}:CO_3^{2+} ratio. Features are similar to those shown in (a) and (b), but the geometry of the hillock differs (see text for complete explanation).

6 are averages over that thickness within the subsectors corresponding to the different vicinal faces. The failure to observe a perfectly sharp "step function" at the boundary between subsectors results from the SXRFMA probe geometry (the incident beam strikes the sample surface at 45°), the 10 μm step size, and the fact that the beam penetrates the entire sample thickness. Analyses of this type correctly represent the differential incorporation between subsectors, providing that the microtopography exhibited at the crystal surface was present during the growth of the concentric zones contained within the section. Time equivalence of the portions of the subsectors analyzed is established by the uniform thickness of the section. Therefore, this technique is best suited for larger single crystals that experienced an extended period of spiral growth.

The distribution of trace elements between nonequivalent subsectors was also determined by analysis of sections perpendicular to growth faces (e.g., as shown in Fig. 5). In this case, time equivalence between different subsectors was established from concentric CL zoning. Representative EPMA data for Mn, Mg, and Sr from selected crystals are reported in Table 2, and Mg data from nonequivalent subsectors are shown in Fig. 7. Magnesium is always found to be enriched in subsectors associated with vicinal faces a' and b' and depleted in a and b. The higher Mg concentrations in the a' and b' subsectors sometimes showed considerable variation that was generally not observed in SXRFMA data for Mn and Sr, perhaps because of the greater volume averaging with the latter technique. In summary, Mg and Mn show differential par-

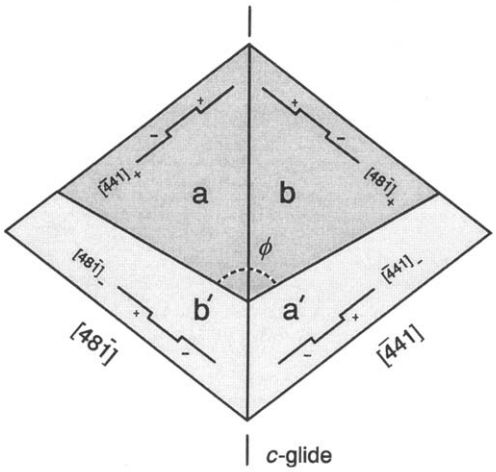

FIG. 4. Schematic diagram showing the geometry of polygonized growth hillocks due to spiral growth on calcite (10$\bar{1}$4). Here, the face appears as bounded by other {10$\bar{1}$4} forms. An a axis is horizontal in the plane of the page, the c-glide is vertical as shown, and the c axis is inclined at ~45° toward the top of the page. Vicinal faces *a* and *b* are symmetrically equivalent to one another, as are *a'* and *b'*. The orientation of growth steps is shown within each vicinal face, and steps and kink sites within steps are labeled by crystallographic direction and sense of movement (see text). The angle ϕ reflects the relative difference in velocity of growth steps on nonequivalent vicinal faces.

titioning behaviors that are similar to one another, but opposite to that for Sr (our preliminary data indicate that Ba shows differential partitioning behavior similar to Sr).

The magnitude of the differential partitioning varies among the trace elements. For Mg and Mn, the difference is typically a factor of 3–4, although considerable variation may exist.

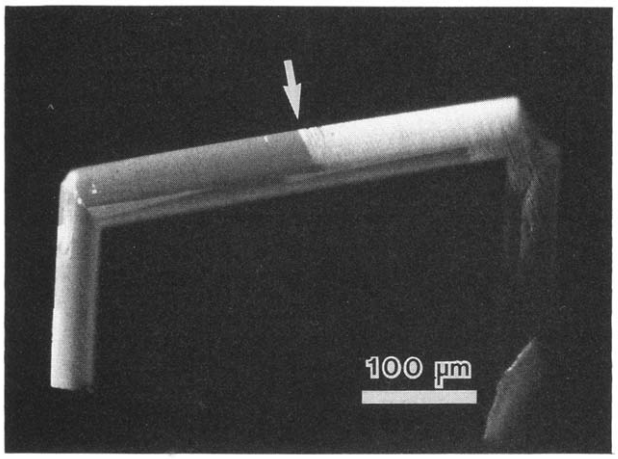

FIG. 5. CL image of a section through a synthetic Mn-doped calcite crystal showing two of the {10$\bar{1}$4} growth sectors. Only the outermost Mn-bearing concentric zone is luminescent. The innermost portions of the sectors grown prior to Mn doping are black. The interface (arrow) within the luminescent concentric zone indicates a sharp difference in Mn concentration between subsectors associated with nonequivalent vicinal faces. The dull portion of the concentric zone corresponds to a subsector grown from vicinal face *a*, and the bright portion corresponds to a subsector grown from vicinal face *b'* (see Fig. 4).

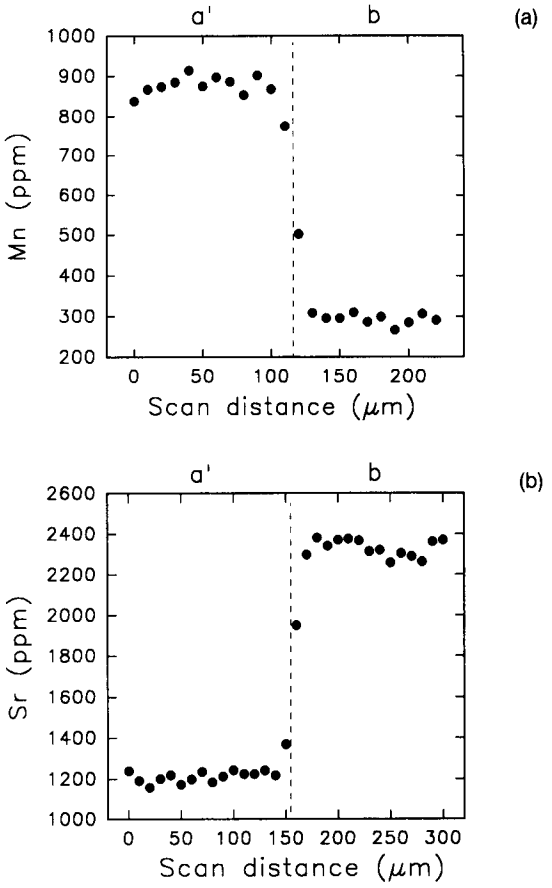

FIG. 6. SXRFMA probe traverses showing the sharp change in (a) Mn and (b) Sr concentrations between time-equivalent portions of subsectors associated with *a'* and *b* vicinal faces. The dashed lines represent the location of the edges separating the nonequivalent vicinal faces (see Fig. 4). Data are from different crystals.

The difference for Mg can be much larger depending on the variations described above. The magnitude of the partitioning difference for Sr is nearly always less than a factor of two and more commonly just a factor of 1.2–1.4.

Variation of microtopography on (10$\bar{1}$4) with solution chemistry

The shape and density of growth hillocks that define the microtopography of (10$\bar{1}$4) growth surfaces are sensitive to the supersaturation and to the Ca^{2+}:CO_3^{2-} ratio of the solution. The morphology of each growth hillock is defined by the shape and orientation of the three or four adjoining vicinal faces, which, in turn, are formed by arrays of steps (Figs. 3, 4). It is important to realize that vicinal faces defined by steps that are parallel, but moving in opposite directions, are not related by the face symmetry of {10$\bar{1}$4} and, therefore, are crystallographically nonequivalent.

The obtuse angle defined by the edges separating adjacent pairs of nonequivalent vicinal faces on each hillock (i.e., the angle ϕ between the different shading patterns in Fig. 4) reflects the relative velocities of growth steps moving in opposite directions. For example, if step velocities were the same on all four vicinal faces, there would be no asymmetry

Table 2. Selected EPMA data[1] for $10\bar{1}4$ subsectors and $01\bar{1}2$ sectors

Mn			
Number[2]	$10\bar{1}4$ subsector		$01\bar{1}2$ sector
	a, b	a', b'	
1	64 (96)	470 (96)	563 (95)
2	75 (81)	483 (106)	--
3	153 (51)	446 (65)	909 (104)
4	213 (86)	341 (86)	--
5	b.d.	274 (122)	480 (69)
6	b.d.	366 (104)	492 (76)

Sr			
Number	$10\bar{1}4$ subsector		$01\bar{1}2$ sector
	a, b	a', b'	
7	1375 (201)	972 (185)	968 (143)
8	1924 (119)	1338 (196)	1332 (144)
9	1488 (165)	1097 (146)	924 (129)
10	1325 (167)	1100 (230)	1052 (134)
11	1882 (174)	1432 (208)	--

Mg		
Number	$10\bar{1}4$ subsector	
	a, b	a', b'
12	5 (24)	193 (60)
13	13 (44)	149 (42)
14	85 (54)	224 (31)
15	66 (31)	250 (40)
16	b.d.	245 (35)
17	5 (271)	216 (130)

Notes:
1. Concentrations in ppm for spot analyses on sections through crystals (see text for details). Estimated errors in parentheses.
2. Number refers to either the pair or trio of spot analyses made in time-equivalent regions of a subsector or sectors of a single crystal.

of the hillocks, and the angle ϕ formed by the intersection of vicinal face pairs a–b' and b–a' would be 180°. However, in all calcite crystals observed, this angle deviates from 180°. For convenience, we measure the angle less than 180° formed on the side containing the a and b vicinal faces, which is found to range between 112–160° among samples grown under different conditions. This deviation indicates that the steps on the a and b vicinal faces always have higher velocities than their parallel but nonequivalent counterparts on vicinal faces a' and b'.

Changes in this angle between nonequivalent vicinal face pairs (and therefore, changes in hillock geometry) must reflect variations in relative step velocities, where increasing deviation from 180° reflects increasing anisotropy. We observed distinct changes in the angle ϕ for crystals from growth experiments with different initial Ca^{2+} concentrations and different Ca^{2+}:CO_3^{2-} ratios (compare Fig. 3a,c). The anisotropy in step velocities on nonequivalent vicinal faces decreased whenever CO_3^{2-} ions were added to solutions, regardless of the initial Ca^{2+} concentrations. To determine if this change was related to the degree of solution supersaturation or to the Ca^{2+}:CO_3^{2-} ratio, crystals were grown from a solution with lower initial Ca^{2+} concentration (0.005 M). Ca^{2+} and CO_3^{2-} ions were then added separately, thereby increasing stepwise the solution supersaturation with respect to calcite. The addition of Ca^{2+} ions consistently increased the anisotropy in step velocities between nonequivalent vicinal faces. The addition of CO_3^{2-} ions, on the other hand, reduced the anisotropy. Furthermore, the most nearly symmetrical four-faced hillocks showing only slight differences in nonequivalent step velocities (i.e., those with the largest angles) were observed only on crystals grown from solutions with relatively low initial Ca^{2+} concentrations (0.005–0.01 M) and $\Omega \approx 10$–12. These observations suggest that, in our solutions, the Ca^{2+}:CO_3^{2-} concentration ratio influenced relative step velocities more strongly than did the degree of supersaturation. However, some anisotropy in step velocities between nonequivalent vicinal faces is evident under all growth conditions in this study.

A large number of growth hillocks commonly appear at higher supersaturation ($\Omega > 15$ in this study). If trace elements are added or the source of CO_3^{2-} ions removed, only a few hillocks eventually dominate the face (Fig. 3), indicating that competition may exist between hillocks.

Another phenomenon observed only at higher supersaturation is the rounding of steps on vicinal faces a' and b' on individual growth hillocks (Fig. 2). In contrast, steps on vicinal faces a and b remain straight over the entire range of solution compositions studied. Although their overall shape changes from pyramidal to semiconical, hillocks always retain their overall symmetry and nonequivalence of step velocities.

{01$\bar{1}$2} rhombohedron

The steep rhombohedron {01$\bar{1}$2} is the dominant form on crystals grown from solutions with high initial Ca^{2+} concentrations (0.1–0.5 M) and moderate pH (7.0–7.3). The growth surface is generally irregular and is dominated by small terraces a few tens of μm wide, which are defined by macrosteps having two step directions both approximately

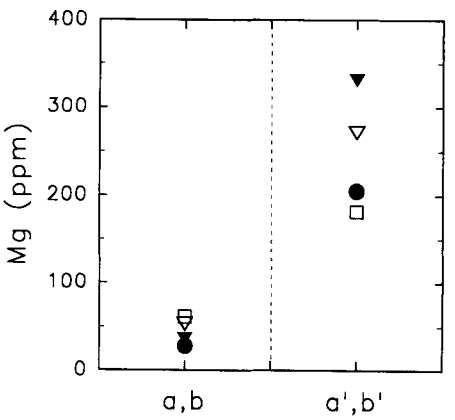

FIG. 7. EPMA spot analyses showing the difference in Mg concentration between time-equivalent portions of $10\bar{1}4$ subsectors associated with nonequivalent vicinal faces (a, b, and a', b') (refer to Fig. 4).

parallel to $\langle 2\bar{2}1 \rangle$. Owing to their orientations, intersecting macrosteps commonly give the appearance of forming pointed hillocks having a single vicinal face, which at its lower slope merges with the overall surface or is interrupted by similar nearby features (Fig. 8). As a result, there is also the appearance of curvature and poorly defined irregular striations parallel to $\langle 010 \rangle$, but macrosteps in that direction are evident on only a few samples (Fig. 8). Because of the curvature, faces are not precisely planar, but commonly deviate slightly from $\{01\bar{1}2\}$, either toward $\{01\bar{1}1\}$ or toward $\{01\bar{1}4\}$, which may exist as a minor shallow rhombohedron.

In crystals grown at supersaturation $\Omega \approx 13$–15, $\{01\bar{1}2\}$ surfaces and corresponding sectors show overall homogeneous CL intensities, indicating that the distribution of Mn^{2+} (and presumably Sr^{2+} and Mg^{2+}) are uniform. At higher supersaturation ($\Omega \approx 20$), sectoral zoning associated with narrow $(10\bar{1}4)$ facets on macrosteps commonly gives the $01\bar{1}2$ sectors a faintly striated appearance in CL (described later).

Other forms

The edges of macrosteps on adjacent $\{01\bar{1}2\}$ faces commonly meet to form $\{11\bar{2}0\}$ prism faces, which are coarsely striated along $\langle 2\bar{2}1 \rangle$ and commonly concave. In such cases, the irregular growth surface of $\{11\bar{2}0\}$ is strongly stepped and consists essentially of symmetry-equivalent $\{01\bar{1}2\}$ facets, alternating in orientation but related by the twofold axes perpendicular to $\{11\bar{2}0\}$. On some crystals, poorly developed $\{11\bar{2}0\}$ faces exist due to pile-up of steps on adjacent $\{10\bar{1}4\}$ faces. These faces are coarsely striated along $\langle \bar{4}41 \rangle$ and commonly curved. In all cases, however, individual $11\bar{2}0$ sectors show homogeneous CL intensities.

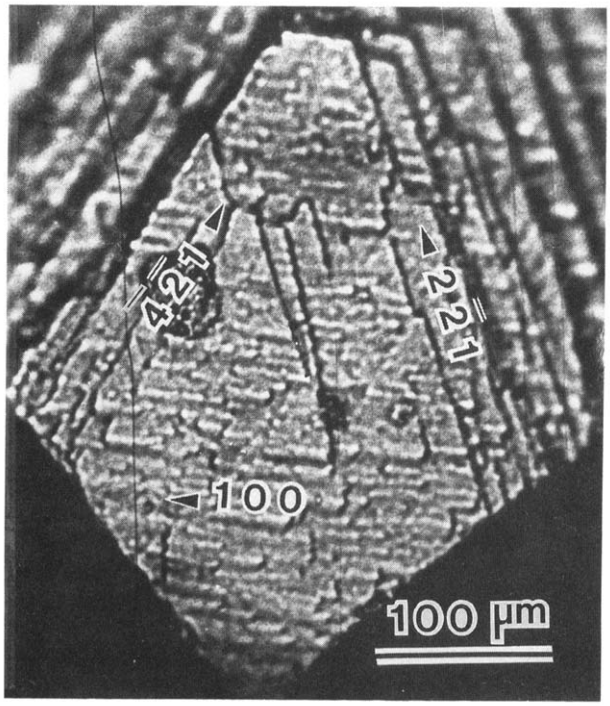

FIG. 8. Optical micrograph of a growth face approximately parallel to $(01\bar{1}2)$ of a synthetic calcite crystal. The microtopography is dominated by $\langle 2\bar{2}1 \rangle$ macrosteps that intersect to form pointed hillocks with a single vicinal face. Macrosteps parallel to [100] truncate the hillocks on this sample, but are absent on most $(01\bar{1}2)$ growth surfaces.

Other minor forms noted on the synthetic crystals include the $\{04\bar{4}1\}$ and $\{01\bar{1}4\}$ rhombohedra, the $\{10\bar{1}0\}$ prism, and the $\{0001\}$ pinacoid. Their growth surfaces and growth sectors all show homogeneous CL intensities.

Sectoral Zoning

Inasmuch as sectoral zoning was not the principal focus of this study, compositional differences between sectors were only assessed for $10\bar{1}4$ and $01\bar{1}2$ sectors, and only Mn and Sr were considered. Representative data for several experiments are given in Table 2. When comparing intersectoral differences involving sectors that also show intrasectoral differences, individual subsectors must be considered. This obviously applies to the calcite crystals studied here. In general, the Mn concentrations in $01\bar{1}2$ sectors are different from those in time-equivalent portions of both of the different subsectors within $10\bar{1}4$ sectors. Strontium concentrations in $01\bar{1}2$ sectors are generally different from those in a and b subsectors, but are not noticeably different from those in the a' and b' subsectors. On average, $01\bar{1}2$ sectors are enriched in Mn and depleted in Sr relative to $10\bar{1}4$ sectors.

Relationship of Macrosteps to Growth Rate and Compositional Zoning

During layer growth, steps commonly "pile-up" or coalesce to form macrosteps. These may be a few multiples of fundamental step heights or much larger, exceeding several μm. Macrosteps are common on all forms on our synthetic calcite crystals. On $\{10\bar{1}4\}$ faces showing the most nearly symmetrical growth hillocks, macrosteps commonly develop on all four vicinal faces. Their height does not exceed a few μm, as judged from CL photographs of sections at high angles to $\{10\bar{1}4\}$ faces, and are generally much lower. Macrosteps on more asymmetric hillocks occur preferentially on the a and b vicinal faces (Fig. 3), where the lateral distance between steps is expected to be larger than on the nonequivalent a' and b' vicinal faces.

Higher macrosteps (up to several tens of μm) are particularly well developed on $\{01\bar{1}2\}$ faces. Differential Mn incorporation at these macrosteps commonly results in sectoral zoning visible in thin section. They form narrow growth sectors with distinct CL intensities within the host $01\bar{1}2$ sector. They are similar in appearance and origin to the "type II striations" described in semiconductor crystals by Bauser and Strunk (1984), and also observed in dolomite by Fouke and Reeder (1992). CL intensities of these narrow sectors are identical to those in fully developed $10\bar{1}4$ sectors. The morphology of these narrow $10\bar{1}4$ sectors associated with the macrosteps on $\{01\bar{1}2\}$ indicates that the macrosteps migrate very slowly across the face during growth. Consequently, the macrosteps behave as small surfaces whose growth kinetics and trace element partitioning affinities are distinct from those of the overall face on which they occur.

DISCUSSION

The exact correlation of trace element distribution patterns with microtopographically defined regions on a crystal sur-

face indicates a mechanistic or path-dependent control on trace element incorporation during growth. In the case of intrasectoral zoning, differences in trace element incorporation are associated with nonequivalent vicinal faces of growth hillocks, which are distinguished by the orientation of the growth steps comprising them. Thus for spiral growth, and perhaps layer growth in general, the specific affinities for trace element incorporation are associated with the detailed structural character of growth steps and the individual incorporation sites (i.e., kink sites) within them. The observation that lateral spreading rates are step specific also indicates a control by structurally different incorporation sites. Hence, there is a need to consider not only the detailed structural character of the multiple incorporation sites but also the relationship between bulk crystal structure and their occurrence and distribution on the surface. However, the existence of surface-controlled zoning and kinetics is limited largely by the presence of different faces and the growth mechanisms that may operate on them.

Periodic Bond Chains and Growth Microtopography

The Periodic Bond Chain (PBC) model of Hartman and Perdok (1955) provides a satisfactory explanation for the orientation of growth steps and allowed growth mechanisms on different faces in terms of the bulk crystal structure. PBCs are defined by the continuous stoichiometric linkage of strongest bonds, i.e., those occurring in the first coordination sphere of the growth units (Hartman, 1987). Crystal faces can be considered to have flat, stepped, or kinked character on the basis of the number of PBCs contained in elementary growth slices (usually defined as slabs of crystal having a thickness equal to the interplanar spacing of the corresponding planes). Elementary growth slices parallel to flat (F) faces contain at least two nonparallel PBCs and such faces are capable of growing

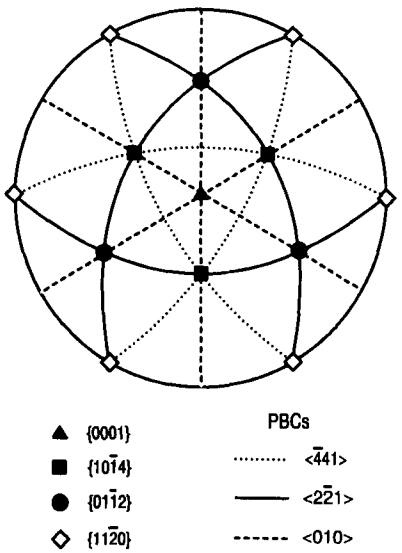

FIG. 9. [001] stereographic projection showing the orientation of PBCs with respect to common growth forms observed on calcite. PBCs are represented as the great circle (i.e., the plane) normal to the PBC direction. F forms are then identified as the intersection of two or more nonparallel PBCs that lie within the corresponding slice.

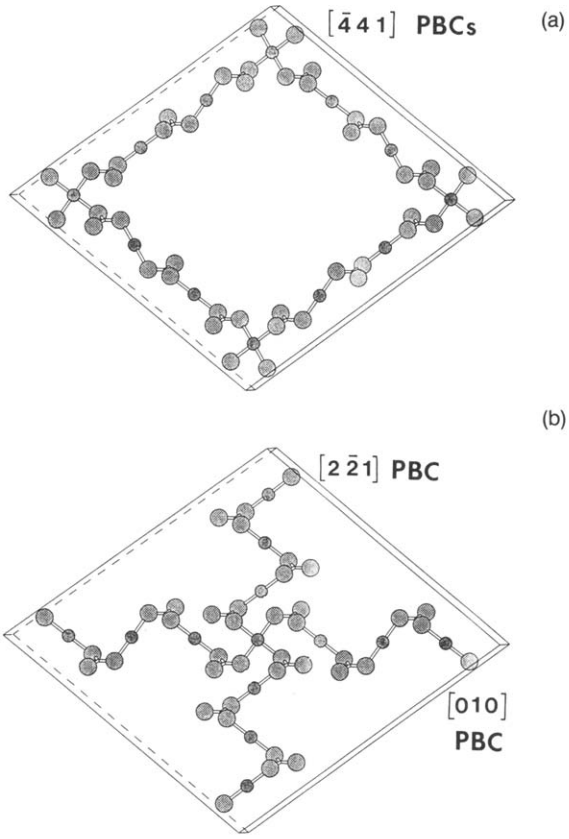

FIG. 10. The 3 Å-thick (10$\bar{1}$4) growth slice showing (a) the two nonparallel ⟨4$\bar{4}$1⟩ PBCs that define the edges for the {10$\bar{1}$4} rhombohedron and (b) the ⟨2$\bar{2}$1⟩ and ⟨010⟩ PBCs that are parallel to the short and long diagonals, respectively, of the rhombohedron. Only atoms in individual PBCs are shown.

by a layer-spreading mechanism. Because attachment of growth units is energetically favored at kink sites along steps, the nucleation of new growth layers is much slower than their lateral migration. As a result, the rate of layer spreading (step velocity) on F faces is much higher than the growth rate normal to the face. Growth on F faces commonly occurs by a spiral mechanism where emergence of a screw dislocation (or the presence of an inclusion) provides a continuous source of steps, obviating the need for nucleation of new layers (Burton et al., 1951). Since attachment energies are highest along PBC directions, growth layers are commonly bounded by relatively straight steps aligned parallel to PBCs within the slice. However, as described below, growth steps may also be curved under certain conditions.

Growth slices parallel to stepped (S) faces contain a single PBC. Their growth surface consists of steps, parallel to this PBC, along which growth rates are rapid. Growth, however, is slower along other directions across the face, which correspond to weaker bonds and thus, lower attachment energies. As a result, S faces have higher normal growth rates than F faces. Growth slices of kinked (K) faces contain no PBC. Their growth surface consists predominantly of kinks, resulting in continuous growth, in which the growth rate normal to the face is faster than for either F or S faces. Therefore, S and

K faces are absent from equilibrium crystal morphologies (Hartman, 1987).

A PBC analysis of calcite by Heijnen (1985) shows that the calcite structure contains three nonequivalent PBCs oriented along $\langle\bar{4}41\rangle$, $\langle 2\bar{2}1\rangle$, and $\langle 010\rangle$. Their mutual orientations with reference to several growth forms are shown in Fig. 9, and they represent the most probable directions of straight growth steps on the face slices in which they lie. The allowed growth mechanisms for any form, however, depend on the specific relationship of its growth slice to these PBCs. We consider only $\{10\bar{1}4\}$, the dominant form, in detail here.

$\{10\bar{1}4\}$ Rhombohedron

The $(10\bar{1}4)$ growth slice, of thickness 3.03 Å, contains all three nonequivalent PBCs noted above. Of these, two nonparallel but symmetrically equivalent $\langle\bar{4}41\rangle$ PBCs occur within the slice, so that four different directions of PBCs can be identified on this F form (Fig. 10).

The relative stability of steps parallel to nonequivalent PBCs was not addressed by Heijnen (1985), but such steps can be qualitatively treated as two-dimensional analogs of F and S faces. PBCs parallel to $\langle\bar{4}41\rangle$ are relatively straight chains of bonds. PBCs parallel to $\langle 2\bar{2}1\rangle$ and $\langle 010\rangle$ directions, on the other hand, consist of undulating bond chains, and, in theory, steps parallel to them should be inherently rougher; i.e., they present a higher density of kink sites. Conversely, steps parallel to the straighter $\langle\bar{4}41\rangle$ PBCs should display relatively lower kink densities and, accordingly, at a given supersaturation should migrate more slowly across the surface than steps parallel to the more undulating PBCs. One may expect that faster lateral migration of steps having higher kink density would cause them to "outgrow" themselves at the edge of growth layers, in a manner similar to that of fast-growing faces relative to slower-growing ones on a crystal.

This reasoning is in agreement with our microtopographic observations of $\{10\bar{1}4\}$ surfaces, which show steps parallel to the two symmetrically equivalent $\langle\bar{4}41\rangle$ PBC directions; these are also the step directions observed by Reeder and Hochella (1991) and by Gratz et al. (1993) using AFM.

The orientation of steps in relation to the symmetry element(s) of a crystal face can impose further constraints on the growth mechanism. The *c*-glide in calcite constrains certain steps parallel to $\langle\bar{4}41\rangle$ to be structurally identical to one another. However, no symmetry element relates steps parallel to a given $\langle\bar{4}41\rangle$ direction but moving in opposite directions (e.g., the steps on vicinal faces *a* and *a'* in Fig. 4 are parallel, but migrate in opposite directions). Regrettably, calculations presented by Heijnen (1985) do not address differences in step energies that must arise from the low face symmetry of $(10\bar{1}4)$. The inability of the PBC theory to account for step-specific kinetics has also been noted by Hottenhuis and Lucasius (1989). Yet, structural differences between nonequivalent steps parallel to the same PBC clearly give rise to the difference in their velocities on nonequivalent vicinal faces observed in our work and also noted by Gratz et al. (1993), and, in doped calcite, to their difference in trace element affinities.

Model kink site geometries on $(10\bar{1}4)$

Because the origin of step-specific kinetics and step-specific trace element incorporation must reflect structural differences, it is necessary to consider the detailed atomic configuration of incorporation sites (i.e., kink sites) in the growth steps observed on $(10\bar{1}4)$. The model presented here is based on an unrelaxed and unreconstructed surface and therefore, should be considered as no more than a first approximation of the actual surface. It is conceptually similar to the model suggested for anion incorporation sites by Staudt et al. (1994), who also discussed its limitations. Here, we assume that Mg^{2+}, Mn^{2+}, and Sr^{2+} are incorporated only into the Ca site. During growth from aqueous solution, the calcite surface is hydrated, and on the basis of current models for surface complexation (e.g., Davis and Kent, 1990; Van Cappellen et al., 1993), surface functional groups are expected to exist. However, the structural role of such functional groups at steps and kink sites is not clear, although future work may elucidate their influence. Therefore, in our first-order model, we assume that the structure-bound atoms are primarily responsible for structural controls on incorporation.

In the bulk structure, layers of Ca atoms alternate with layers of CO_3 groups along the *c* axis. There is a single Ca site, and its coordination environment in the bulk structure is a trigonally elongated octahedron with each of the six O atoms at the corners belonging to a separate CO_3 group (cf. Reeder, 1983). The basal edges of the octahedron (3.26 Å) are slightly shorter than the lateral edges (3.41 Å). When we consider the coordination environment of Ca within a $(10\bar{1}4)$ slice, it is important to recognize that such a slice is inclined at 45° with respect to the *c* axis. Consequently, different CO_3 groups and Ca atoms within a $(10\bar{1}4)$ slice lie at different heights, within different carbonate and Ca layers perpendicular to the *c* axis. As this relationship is important for understanding the detailed coordination of incorporation sites, we are careful to distinguish between layers of the bulk structure (i.e., Ca and carbonate layers perpendicular to *c*) and the $(10\bar{1}4)$ slices (inclined at 45° to *c*). In an isolated $(10\bar{1}4)$ slice, corresponding to an elementary growth layer (3Å thick), each Ca atom is coordinated to four nearest-neighbor O atoms, each from a CO_3 group within the slice. For the same slice at the surface of a crystal, the Ca is also coordinated to one O atom from the $(10\bar{1}4)$ slice below. However, at a kink site within an elementary growth step (cf. Fig. 4), the nearest-neighbor coordination of a Ca (or another metal ion substituting for it) is only three O atoms—always two within the surface slice containing the kink site and one in the parallel slice below (Fig. 11).

We distinguish between growth steps that are parallel but moving in opposite directions in the manner described by Staudt et al. (1994), by adding + or − subscripts to the direction parallel to the step. The four distinct steps on a $(10\bar{1}4)$ face (shown in Fig. 4) are $[\bar{4}41]_+$, $[\bar{4}41]_-$, $[48\bar{1}]_+$, and $[48\bar{1}]_-$. Two elementary kink sites can be identified in each of these four steps, resulting in eight distinct kink sites (Fig. 4). Symmetry (i.e., the *c*-glide) reduces these to four sites in which the coordination environment is actually different. In a given step, the two kink sites differ in the direction in which they translate during growth. Using the same nota-

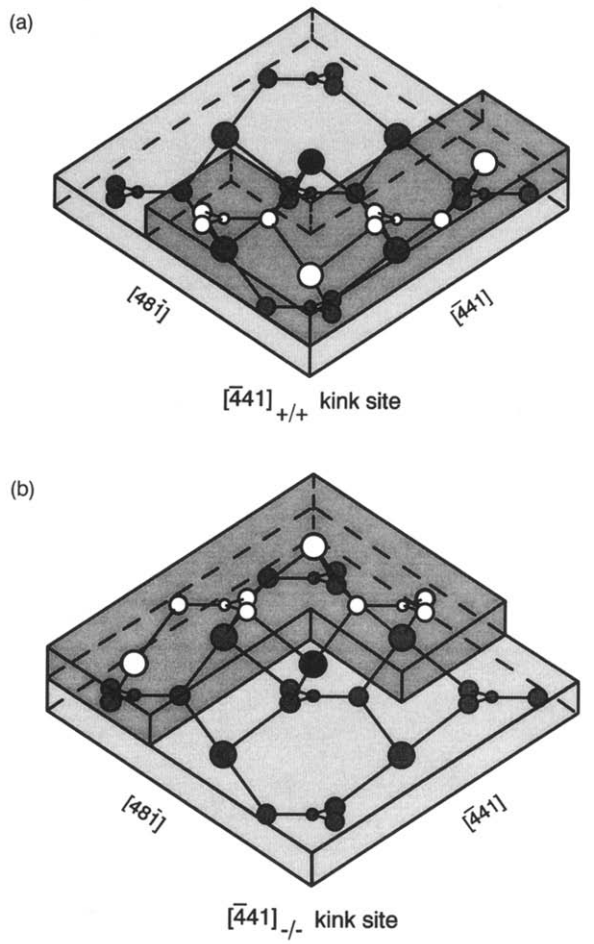

FIG. 11. Model cation kink sites shown in perspective for incorporation of divalent trace metals into growth steps on the calcite ($10\bar{1}4$) face. (a) the $[\bar{4}41]_{+/+}$ kink site and (b) the $[\bar{4}41]_{-/-}$ kink site. The *c* axis is inclined at 10° from the top of the page and one *a* axis is horizontal on the page. Small, medium, and large circles represent C, O, and Ca atoms, respectively. Open circles denote atoms that lie within the upper ($10\bar{1}4$) slice (dark shading), and hatched circles denote atoms that lie within the lower slice (light shading). The solid black circle represents an ion occupying the cation kink site. Since the slice orientation is 45° from the *c* axis, atoms within a slice lie within different calcium and carbonate layers of the bulk structure (i.e., alternating along *c*). Different carbonate layers are readily identified by the orientation of the CO_3 groups. The ion in the kink site is coordinated by three O atoms, each belonging to a separate CO_3 group. In (a), the three coordinating O atoms lie within the same carbonate layer of the bulk structure, whereas in (b) the three O atoms lie within adjacent carbonate layers, causing the geometry and "size" of the sites to differ. See text for further explanation.

tion as Staudt et al. (1994), we distinguish between the kink sites in a given step by assigning an additional + or − subscript to the step designation. Consequently, $[\bar{4}41]_{+/+}$ and $[\bar{4}41]_{+/-}$ are the two kink sites in the $[\bar{4}41]_+$ step, but they translate in opposite directions along the length of the step.

In order to illustrate our analysis, the nearest-neighbor and next-nearest neighbor coordination of the $[\bar{4}41]_{+/+}$ and $[\bar{4}41]_{-/-}$ kink sites are shown in Fig. 11a and b. In each figure, two 3 Å-thick ($10\bar{1}4$) slices defining the kink sites are shown by different shading. In Fig. 11a, the kink site faces away from the viewer and in Fig. 11b, toward the viewer. In each case, the kink site is centered at the position of a Ca site. The "ion" residing in the kink site is indicated as a solid black circle. Calcium atoms and CO_3 groups that lie within the top slice are represented as unshaded circles, whereas those within the lower slice are hatched. The first-shell coordination between existing atoms in the slices is shown by "stick bonds".

Inspection of Fig. 11a and b readily shows that the "size" and the geometry of the coordination environments differ between these kink sites. In the $[\bar{4}41]_{+/+}$ kink site (Fig. 11a), the three O atoms that form the primary coordination of the site lie within the same carbonate layer (perpendicular to the *c* axis) and, by reference to the Ca octahedron in the bulk, are separated from one another by 3.26 Å. In contrast, the three coordinating O atoms in the $[\bar{4}41]_{-/-}$ kink site (Fig. 11b) lie within two adjacent carbonate layers—one in the carbonate layer below and two in the carbonate layer above the kink site. The O-O distance in adjacent carbonate layers is 3.41 Å, and that in the same layer is 3.26 Å; hence, distances separating the coordinating O atoms clearly differ between these two sites. More important, perhaps, is the site geometry relative to the surface. It can be readily seen that the net direction defined by the three bonds from the coordinating O atoms to the substituting ion in the $[\bar{4}41]_{+/+}$ kink site is parallel to [001], or inclined at roughly 45° to ($10\bar{1}4$). In the $[\bar{4}41]_{-/-}$ kink site, however, the directional sum of the three bonds is roughly parallel to ($10\bar{1}4$). All these factors suggest that the $[\bar{4}41]_{+/+}$ kink site is a more open site than $[\bar{4}41]_{-/-}$, with fewer steric constraints on the ion residing in the kink site. Therefore, the $[\bar{4}41]_{+/+}$ kink site should favor incorporation of larger cations, whereas smaller cations should be more easily incorporated in the $[\bar{4}41]_{-/-}$ kink site.

In the $[\bar{4}41]_{+/-}$ and $[\bar{4}41]_{-/+}$ kink sites (not shown here), two of the coordinating O atoms lie in the carbonate layer below the kink site and the third in the layer above, giving a geometry like that of the $[\bar{4}41]_{-/-}$ kink site and favoring incorporation of smaller ions.

Differences among these kink sites also exist in their next-nearest-neighbor coordination with Ca atoms. In the bulk structure, there are twelve Ca atoms comprising a split second coordination shell for the cation site: six at approximately 4 Å and six at 5 Å. In a kink site, this coordination is reduced to six but remains split with three at each distance. Again, inspection reveals that the geometry of the next-nearest-neighbor coordination differs between kink sites. For example, in the $[\bar{4}41]_{+/+}$ kink site, the three nearest Ca atoms (at 4 Å) all lie within the cation layer below that of the kink site. On the other hand, in the $[\bar{4}41]_{-/-}$ kink site, one Ca at 4 Å lies in the cation layer above that of the kink site and two lie in the layer below. In the $[\bar{4}41]_{+/-}$ kink site, the next-nearest-neighbor coordination is similar to that of the $[\bar{4}41]_{+/+}$ kink site, whereas for the $[\bar{4}41]_{-/+}$ kink site, its next-nearest-neighbor coordination is similar to that of the $[\bar{4}41]_{-/-}$ kink site. Although next-nearest-neighbor interactions are presumed to be less important than nearest-neighbor interactions, here, the two are seen to be complementary. Hence, for the two nonequivalent step types considered here, $[\bar{4}41]_+$ and $[\bar{4}41]_-$, two structurally distinct kink sites are predicted in each.

Consideration of these coordination differences, even though strictly qualitative, suggests that ions larger than Ca^{2+} would be more readily incorporated into the geometrically less constrained and "larger" kink sites that occur only in the symmetrically related $[\bar{4}41]_+$ and $[48\bar{1}]_+$ steps. Correspondingly, ions smaller than Ca^{2+} should be preferentially incorporated into the "smaller", more constrained sites in the symmetrically related $[\bar{4}41]_-$ and $[48\bar{1}]_-$ steps. Our observations of differential trace element incorporation are consistent with this analysis. Magnesium and Mn are preferentially incorporated into $[\bar{4}41]_-$ and $[48\bar{1}]_-$ steps, whereas Sr (this study) and Ba (preliminary results) are preferentially incorporated into $[\bar{4}41]_+$ and $[48\bar{1}]_+$ steps.

In view of the size and geometry differences of the kink sites, one might also expect the advance of the $[\bar{4}41]_+$ and $[48\bar{1}]_+$ steps to be less hindered and therefore more rapid, which is consistent with our observed asymmetry of growth hillocks and with the in situ observations of Gratz et al. (1993). Because the anisotropy of step velocities on nonequivalent vicinal faces occurs even in undoped calcite crystals, Ca^{2+} ions are apparently also more readily incorporated into the more open kink sites in $[\bar{4}41]_+$ and $[48\bar{1}]_+$ steps. Staudt et al. (1994) have examined differential incorporation into CO_3 sites on calcite $\{10\bar{1}4\}$ surfaces, with findings that are consistent with our analysis.

As noted, our first-order model ignores any possible surface reconstruction or relaxation. Stipp and Hochella (1991) examined the $(10\bar{1}4)$ cleavage surface of calcite in vacuo using LEED and found that the structure is essentially the same as in the bulk crystal. However, they observed weak extra reflections, which they suggested may be due to slight relaxation of the surface-most CO_3 groups. Recent AFM observations of the $(10\bar{1}4)$ calcite surface in air and in water (Stipp et al., 1994) also raise the possibility of some restructuring, although it remains unclear how such observations may relate to an incorporation site. Nevertheless, at the vicinity of a kink site, we would anticipate any relaxation to be strongly constrained by the coordination. Therefore, if relaxation is important, the differences in coordination that we predict on the basis of an unrelaxed model should be reflected by corresponding differences in a relaxed surface, and, qualitatively, our model should retain some merit. Moreover, our observation that growth hillock geometry and differential incorporation patterns for all trace elements studied are consistent with the symmetry of the unrelaxed surface lends support for application of an unrelaxed surface site model.

Step roughening on $\{10\bar{1}4\}$

The selective rounding of steps on $\{10\bar{1}4\}$ surfaces grown at higher supersaturation demonstrates another example of step-specific kinetics that merits attention. The rounding of polygonal growth hillocks at high supersaturations and high growth rates has been documented in several types of crystals (Sunagawa, 1984). In calcite crystals grown at initial Ca concentrations of 0.005–0.1 M and $\Omega \approx 15$–18, rounding of steps was observed only on the a' and b' vicinal faces of hillocks. The overall density of kink sites in steps is generally expected to increase with the saturation state during solution growth, giving rise to "rough" steps (e.g., Ohara and Reid, 1973). Steps on vicinal faces a and b (Fig. 4) with higher overall growth rates should be more efficient at "burying" kink sites and preserving straight orientations than steps on a' and b' growing more slowly, although with the same PBC directions. Thus, it is evident that the differences in growth hillock morphology occur in response to differences in fluid composition, but the details of the transition are controlled by the step structure.

$\{01\bar{1}2\}$ Steep Rhombohedron

The absence of differential incorporation of trace elements on $\{01\bar{1}2\}$ faces can be explained on the basis of the observed microtopography and the corresponding slice structure. Heijnen (1985) noted that an elementary $(01\bar{1}2)$ growth slice contains both interconnected $\langle 2\bar{2}1\rangle$ PBCs and interconnected $\langle 010\rangle$ PBCs, each defining $\{01\bar{1}2\}$ as an F form. Our observations, however, show that $\{01\bar{1}2\}$ faces are generally nonplanar (cf. Kirov et al., 1972), and the microtopography is dominated by macrosteps (and presumably, elementary growth steps) in two orientations, both parallel to the $\langle 2\bar{2}1\rangle$ PBCs. Growth steps parallel to [010] may exist, but macrosteps are not common. Thus, the dominant growth steps in evidence on $\{01\bar{1}2\}$ are structurally equivalent, being related by the c-glide symmetry element of the $\{01\bar{1}2\}$ faces. Consequently, in these crystals differential incorporation of trace elements is not expected within $01\bar{1}2$ sectors, in agreement with our observations. Further work is clearly indicated for this important form—specifically, to determine the presence of $\langle 010\rangle$ steps, which would be nonequivalent with $\langle 2\bar{2}1\rangle$ steps. Moreover, we cannot preclude that $\{01\bar{1}2\}$ might grow as an F form (with differential incorporation) in different solutions.

Other Forms

$\{11\bar{2}0\}$ and $\{0001\}$, also present as minor forms on some of our synthetic calcite crystals, are, respectively, S and K forms according to PBC analysis. The $\{11\bar{2}0\}$ growth surfaces show macrosteps parallel to $\langle 2\bar{2}1\rangle$ PBCs, or less commonly parallel to $\langle\bar{4}41\rangle$ PBCs. Steps parallel to either PBC, but moving in opposite directions, are related by the twofold axis perpendicular to the $\{11\bar{2}0\}$ growth surface. Therefore, they are expected to show equivalent kinetics and preferences for trace element incorporation, in agreement with observation.

The (0001) growth slice contains only partial $\langle 010\rangle$ PBCs, and its surface should consist of kinks (K face). This is consistent with its irregular surface microtopography and homogeneous CL.

Sectoral Zoning

Although little consideration has been given to sectoral zoning in this paper, it seems important to comment on its relationship to intrasectoral zoning. It should be evident that wherever intrasectoral zoning exists in a crystal containing nonequivalent sectors, then sectoral zoning must also exist. However, the opposite is clearly not true, as many examples of sectorally zoned minerals fail to show intrasectoral zoning. Paquette and Reeder (1990) suggested that sectoral zoning

has an origin similar to intrasectoral zoning, since growth steps occurring on nonequivalent faces, even if parallel to the same PBC, generally have different structural characteristics and may present kink sites that differ in their detailed geometry and coordination and, therefore, in their affinities for foreign ions. Moreover, growth mechanisms may differ between nonequivalent faces, particularly if the faces in question are of different type (e.g., F and S faces of the PBC theory).

CONCLUDING REMARKS

Presently, the significance of these findings is probably more important for understanding how growing crystals differentiate among and incorporate elements rather than for immediate application as a petrologic tool. In our view the observations emphasize the importance of the mechanistic aspects of the growth process. Crystal growth can be viewed as the advancement of an interface as units attach to it. What becomes evident is that the structural details of the interface and the manner in which it advances are important for controlling the distribution and concentration of elements that are left behind to form the bulk crystal.

Our findings also suggest a slightly different way in which the influence of bulk crystal structure is manifested on trace element compatibility. Whereas trace element size, charge, and electronic properties have traditionally been compared to host ions residing in sites in the bulk structure, we emphasize the surface sites at which incorporation occurs. The bulk crystal structure, however, constrains the available growth mechanisms and largely controls the surface microtopography, specifically, the orientation and structure of growth steps and kink sites. The detailed geometry and coordination of kink sites, in turn, controls element preferences for incorporation as well as incorporation kinetics. In calcite, the anisotropy of the bulk structure that is expressed at the surface results in different attachment energies at nonequivalent kink sites, and this is the fundamental cause of site-specific kinetics. The understanding that nonequivalent surface sites may be spatially segregated on a face by a particular growth mechanism provides new insight, not only for trace element partitioning, but also for the extensive morphological variation characteristic of natural calcite crystals.

Our demonstration that step-specific kinetics and trace element affinities for calcite surfaces are consistent with face symmetry suggests that a knowledge of face symmetry elements can be used to predict whether differential incorporation may occur within any given sector. Any such prediction clearly carries the assumption that little or no surface reconstruction or relaxation has occurred, and that remains a question for most mineral surfaces. However, we note that recent studies of surface-controlled incorporation of trace elements in natural topaz (Northrup and Reeder, 1994), in natural apatite (Rakovan and Reeder, 1994), and for complex anions in calcite (Staudt et al., 1994) all show that growth hillocks and associated distributions of trace elements are consistent with face symmetry.

Because of the emphasis on structure and mechanism, we have given little consideration to the actual values of trace element partition coefficients in this work. In fact, the more important conclusion is that the absolute value of any empirical partition coefficient is dependent on the detailed configuration of available incorporation sites, which may vary over the surface of a crystal and with external conditions of growth. In view of this path dependence, experimentally determined trace element distributions are unlikely to represent equilibrium ones. Future geochemical applications based on trace element partitioning must take these findings into consideration, especially in view of the increasing reliance on instrumental techniques having superior spatial and analytical resolution.

Acknowledgments—We thank W. Bruce Ward, C. F. Woensdregt, John Rakovan, Wilfried Staudt, and Paul Northrup for valuable discussions. Roger A. Mason, Nicholas E. Pingitore, and an anonymous reviewer offered helpful comments on the manuscript. Steve Sutton, Mark Rivers, and Saša Bajt provided essential help with SXRFMA at the National Synchrotron Light Source, Brookhaven National Laboratory. Funding was provided by NSF grants EAR9003915 and EAR9204809.

Editorial handling: R. C. Burruss

REFERENCES

Bauser E. and Strunk H. P. (1984) Microscopic growth mechanisms of semiconductor: Experiments and models. *J. Crystal Growth* **69,** 561–580.

Burton W. K., Cabrera N., and Frank F. C. (1951) The growth of crystals and the equilibrium structure of their surfaces. *Roy. Soc. London Phil. Trans.* **A243,** 299–358.

Busenberg E. and Plummer L. N. (1985) Kinetic and thermodynamic factors controlling the distribution of SO_4^{2-} and Na^+ in calcites and aragonites. *Geochim. Cosmochim. Acta* **49,** 713–725.

Davis J. A. and Kent D. B. (1990) Surface complexation modeling in aqueous geochemistry. In *Mineral-Water Interface Geochemistry* (ed. M. F. Hochella and A. F. White); *Rev. Mineral.* **23,** pp. 177–260.

Dove P. M. and Hochella M. F., Jr. (1993) Calcite precipitation mechanisms and inhibition by orthophosphate: In situ observations by scanning force microscopy. *Geochim. Cosmochim. Acta* **57,** 705–714.

Dowty E. (1989) *ATOMS. A Computer Program for Displaying Atomic Structures.* Shape Software.

Dromgoole E. L. and Walter L. M. (1990) Iron and manganese incorporation into calcite: Effects of growth kinetics, temperature and solution chemistry. *Chem. Geol.* **81,** 311–336.

Fouke B. W. and Reeder R. J. (1992) Surface structural controls on dolomite composition. *Geochim. Cosmochim. Acta* **56,** 4015–4024.

Gratz A. J., Hillner P. E., and Hansma P. K. (1993) Step dynamics and spiral growth on calcite. *Geochim. Cosmochim. Acta* **57,** 491–495.

Gruzensky P. M. (1967) Growth of calcite crystals. In *Crystal Growth* (ed. H. S. Peiser), pp. 367–367. Pergamon.

Hartman P. (1987) Modern PBC theory. In *Morphology of Crystals: Part A* (ed. I. Sunagawa), Chap. 4, pp. 269–329. Terra.

Hartman P. and Perdok W. G. (1955) On the relations between structure and morphology of crystals. *Acta Crystall.* **8,** 49–52.

Heijnen W. M. M. (1985) The morphology of gel grown calcite. *N. Jb. Miner. Mh.* **1985,** 357–381.

Hendry J. P. and Marshall J. D. (1991) Disequilibrium trace element partitioning in Jurassic sparry calcite cements: Implications for crystal growth mechanisms during diagenesis. *J. Geol. Soc. London* **148,** 835–848.

Hottenhuis J. and Lucasius C. B. (1989) Influence of internal crystal structure on surface morphology; in-situ observations of potassium hydrogen phthalate {010}. *J. Crystal Growth* **94,** 708–720.

Kirov G. V., Vesselinov I., and Cherneva Z. (1972) Conditions of formation of calcite of tabular and acute rhombohedral habit. *Kristall und Tech.* **7,** 497–509.

Lorens R. B. (1981) Sr, Cd, Mn and Co distribution in calcite as a function of calcite precipitation rate. *Geochim. Cosmochim. Acta* **45,** 553–561.

Lu F. Q., Smith J. V., Sutton S. R., Rivers M. L., and Davis A. M. (1989) Synchrotron X-ray fluorescence analysis of rock-forming minerals, 1. Comparison with other techniques; 2. White-beam energy-dispersive procedure for feldspars. *Chem. Geol.* **75,** 123–143.

Morse J. W. and Bender M. L. (1990) Partition coefficients in calcite: Examination of factors influencing the validity of experimental results and their application to natural systems. *Chem. Geol.* **82,** 265–277.

Mucci A. and Morse J. W. (1983) The incorporation of Mg^{2+} and Sr^{2+} into calcite overgrowths: influences of growth rate and solution composition. *Geochim. Cosmochim. Acta* **47,** 217–233.

Northrup P. A. and Reeder R. J. (1994) Evidence for the importance of growth-surface structure to trace element incorporation in topaz. *Amer. Mineral.* **79,** 1167–1175.

Ohara M. and Reid R. C. (1973) *Modeling Crystal Growth Rates from Solution.* Prentice-Hall.

Paquette J. (1991) Crystallographic controls on impurity incorporation in calcite. Ph.D. dissertation, State Univ. New York at Stony Brook.

Paquette J. and Reeder R. J. (1990) New type of compositional zoning in calcite: Insights into crystal-growth mechanisms. *Geology* **18,** 1244–1247.

Paquette J., Ward W. B., and Reeder R. J. (1993) Compositional zoning and crystal growth mechanisms in carbonates: A new look at microfabrics imaged by cathodoluminescence microscopy. In *Carbonate Microfabrics* (ed. R. Rezak and D. Lavoie), Chap. 18, pp. 243–252. Springer-Verlag.

Pingitore N. E. and Eastman M. P. (1986) The coprecipitation of Sr^{2+} with calcite at 25°C and 1 atm. *Geochim. Cosmochim. Acta* **50,** 2195–2203.

Rakovan J. and Reeder R. J. (1994) Differential incorporation of trace elements and dissymmetrizatio in apatite: The role of surface structure during growth. *Amer. Mineral.* **79,** 892–903.

Raven M. J. and Dickson J. A. D. (1989) Fir-tree zoning: an indicator of pulsed crystallization in calcite cement crystals. *Sediment. Geol.* **65,** 249–259.

Reeder R. J. (1983) Crystal chemistry of the rhombohedral carbonates. In *Carbonates: Mineralogy and Chemistry* (ed. R. J. Reeder); *Rev. Mineral.* **11,** pp. 1–47.

Reeder R. J. and Grams J. C. (1987) Sector zoning in calcite cement crystals: Implications for trace element distributions in carbonates. *Geochim. Cosmochim. Acta* **51,** 187–194.

Reeder R. J. and Hochella M. F., Jr. (1991) Atomic force microscopy of calcite growth surfaces. *GSA Ann. Mtg.,* **A216** (abstr.).

Reeder R. J. and Paquette J. (1989) Sector zoning in natural and synthetic calcites. *Sediment. Geol.* **65,** 239–247.

Reeder R. J., Fagioli R. O., and Meyers W. J. (1990) Oscillatory zoning of Mn in solution-grown calcite crystals. *Earth-Science Rev.* **29,** 39–46.

Somorjai G. A. (1981) *Chemistry in Two Dimensions: Surfaces.* Cornell University Press.

Staudt W. J., Reeder R. J., and Schoonen M. A. A. (1994) Surface structural controls on compositional zoning of SO_4^{2-} and SeO_4^{2-} in synthetic calcite single crystals. *Geochim. Cosmochim. Acta* **58,** 2087–2098.

Stipp S. L. and Hochella M. F., Jr. (1991) Structure and bonding environments at the calcite surface as observed with X-ray photoelectron spectroscopy (XPS) and low energy diffraction (LEED). *Geochim. Cosmochim. Acta* **55,** 1723–1736.

Stipp S. L., Eggleston C. M., and Nielsen B. S. (1994) Calcite surface structure observed at microtopographic and molecular scales with atomic force microscopy (AFM). *Geochim. Cosmochim. Acta* **58,** 3023–3033.

Sunagawa I. (1984) Growth of crystals in nature. In *Materials Science of the Earth's Interior* (ed. I. Sunagawa), pp. 63–105. Terra.

Van Cappellen P., Charlet L., Stumm W., and Wersin P. (1993) A surface complexation model of the carbonate mineral-aqueous solution interface. *Geochim. Cosmochim. Acta* **57,** 3505–3518.

Wolery T. J. (1983) EQ3NR. *A Computer Program for Geochemical Aqueous Speciation-Solubility Calculations: User's Guide and Documentation; UCRL-53414.* Lawrence Livermore Lab.